Supporting Information

Hembury et al. 10.1073/pnas.1419622112

SI Materials Synthesis

Polystyrene Particles. Polystyrene particles were prepared using emulsion polymerization with an anionic initiator, potassium persulfate (KPS), as described in a recent publication (1). Dihexylsulfosuccinate sodium salt (2.6 g), MilliQ H_2O (206 mL), sodium bicarbonate (0.43 g), and styrene (30.2 g) were mixed in a round-bottom flask. The solution was degassed over 30 min by bubbling with argon. The solution was then added to a preheated 90 °C oil bath. Because styrene can autoinitiate at this temperature, the initiator, KPS (0.43 g) in MilliQ H_2O (14.9 mL), was promptly added to the hot solution via syringe. The reaction was performed under a slight positive pressure of argon. After 6 h the reaction was complete. The particles were dialyzed over 1 wk, producing a polystyrene dispersion.

Hollow Mesoporous Silica Shells. Mesoporous silica was grown on the polystyrene particles to produce a core cavity and obtain hollow mesoporous silica shells (HSs), as described in a recent publication (1). The surfactant, hexadecyltrimethylammonium bromide (CTAB, 3.2 g), was dissolved in MilliQ H_2O (100 mL) at 35 °C. The polystyrene particles (17.5 g) were diluted with 500 mL MilliQ H_2O and 200 mL of ethanol and basified with 7.5 g of 28% ammonia. The CTAB/H_2O was added to the polystyrene dispersion and allowed to equilibrate for 45 min. Tetraethyl orthosilicate (TEOS, 5.4 g) was added dropwise to the solution, which was subsequently allowed to react for 1 d. To collect the particles, the solution was centrifuged at 6,797 × *g* for 1 h. The resulting material was calcined using the following program: 25–250 °C at a rate of 5 °C min^{-1}, held at 250 °C for 2 h followed by 250–550 °C at a rate of 2 °C min^{-1}, held at 550 °C for 5 h.

NQR Synthesis. NQRs were synthesized to deconvolute the contribution of AuQDs and AuNPs in contributing to the photonic properties of the QRs. The same protocol used for the QRs was used for the NQRs with the exceptions that nonhollow Stöber mesoporous silica particles (NHSs) with the same pore size as the HSs were used instead of HSs. The NHSs were prepared using the following procedure: 0.33 g CTAB was dissolved in 60 g MilliQ water and 16 g of ethanol and basified with 0.75 g of 28% ammonia. TEOS (5.0 g) was added dropwise to the solution, which was subsequently allowed to react for 1 d. To collect the material, the solution was centrifuged at 6,797 × *g* for 20 min. Materials were calcined using the following program: 25–250 °C at a rate of 5 °C per min, held at 250 °C for 2 h, 250–550 °C at a rate of 2 °C per min, held at 550 °C for 5 h.

SI Particle Morphology and Composition

Small-angle X-ray scattering (SAXS) was collected on a Rigaku S-Max3000 equipped with a microfocus source of 20 × 20 μm. The radiation wavelength (Kα) used was 0.154 nm. A 2D Gabriel-type detector was placed 1,469 mm from the sample. Diffraction patterns were analyzed using SAXGUI V2.04.05 software. Bragg's law was used to calculate the *d* spacing from the SAXS data.

WAXS was collected on the same instrument. The distance between the image plate and the sample was 59.5 mm. The results were analyzed using Image.exe 2001 and a 0.05- × 0.05-mm pixel size. The appearances of peaks in the WAXS spectra corresponded to the crystalline gold JCPDS-ICDD file 04–0784. The Scherrer equation was used to calculate the particle size of the gold crystals. L is the crystallite size, K is the shape factor (0.9), λ is the wavelength of the Cu radiation (0.154 nm), B is the full width at half-maximum in radians, and θ is the Bragg angle:

$$L = \frac{K\lambda}{B\cos\theta}.$$

The nitrogen physisorption method was used to determine the effect of the QR synthesis on the integrity of the silica shell of the QR. The nitrogen adsorption and desorption curves were obtained on a BELSORP-max (BEL Japan) instrument. The samples were degassed at 80 °C at a pressure of 10^{-2} kPa for 1 d before analysis using a BELPREP-vacII (BEL Japan) pretreatment instrument. The adsorption curve was analyzed according to the Barrett Joyner Halenda model to estimate pore size distribution.

TEM was used to determine the morphology and size distribution of the QRs. TEM images of the particles were acquired using a JEOL 2010 TEM equipped with a Gatan camera and an energy-dispersive X-ray spectroscopy detector (Oxford Instrument) operated at an accelerating voltage of 200 kV. Higher-magnification TEM and HAADF-STEM was used to resolve and image gold inside of the QRs pores. High-magnification TEM images and HAADF-STEM images of the particles were acquired on a Gatan camera using a FEI TITAN 80/300 STEM/TEM operated at an accelerating voltage of 200 kV. Samples were dissolved in ethanol (1 mg·mL^{-1}) and drop-deposited on 300-mesh carbon-coated copper TEM grids (Agar Scientific) before analysis.

Ultramicrotomy was used to assess the inner structure of the QRs. The QRs (1 mg) were embedded through a graded Epon812/Araldite resin:acetone series (1:2, 2:1, 1:0 vol/vol), transferred to fresh pure Epon812/Araldite and polymerized at 60 °C for 1 d. Ultrathin sections of ∼100 nm were cut on a Power Tome XL ultramicrotome (RMC Products) using a 45° diamond knife (Diatome) and transferred to a 300-mesh thin bar TEM copper grids (Electron Microscopy Sciences). TEM images were acquired using a JEOL 2000 TEM operated at 120 kV.

EDS analysis was used to quantify the chemical composition of the QRs. X-ray counts were recorded over five separate areas per specimen (in triplicate) during a 1-min period at 10 kV and analyzed using INCA Energy 3000 software (Oxford Instruments). The contribution of each component of the QR (SiO_2 shell, AuQD, and AuNP) to the total mass of one QR was calculated using the EDS data and the following set of equations.

From geometrical considerations, the mass of the silica shell of the QR, m_{SiO2}, and the mass of the AuNPs inside the cavity of the QR, m_{AuNP}, were calculated using

$$m_{SiO2} = \frac{4}{3}\pi\left(r^3_{SiO2outer} - r^3_{SiO2inner}\right)\cdot d_{SiO2}$$

$$m_{AuNP} = \frac{4}{3}\pi r^3_{AuNP}\cdot d_{AuNP},$$

where d_{SiO2} and d_{AuNP} are the densities of mesoporous silica (0.52 g·cm^{-3} obtained from the mesoporous volume of the silica shell measured using nitrogen physisorption) and gold particles (973 g·cm^{-3} obtained by assuming a 0.5 packing factor for gold nanoparticles), respectively. $r_{SiO2outer}$ and $r_{SiO2inner}$ are the outer and inner radius of the silica shell, 75 nm and 50 nm, respectively (as determined from TEM analysis). r_{AuNP} is the radius of the entire aggregate of AuNPs inside the cavity, assuming they

aggregate in a spherical structure of 28-nm diameter (as determined from TEM analysis).

$$\begin{cases} m_{QR} = m_{SiO2} + m_{AuNP} + m_{AuQD} \\ \dfrac{m_{SiO2}}{m_{QR}} = \dfrac{x_{EDS}(SiO2)}{100} \end{cases}$$
$$\Rightarrow m_{AuQD} = \left(\frac{100}{x_{EDS}(SiO2)} - 1\right) \cdot m_{SiO2} - m_{AuNP}.$$

By reinputting m_{AuQD} into the first equation of the previous set of equations, the mass of one QR, m_{QR}, was obtained. The mass percentage of AuQDs and AuNPs was then calculated using

$$\begin{cases} x_{calculated}(AuQD) = \dfrac{m_{AuQD}}{m_{QR}} \\ x_{calculated}(AuNP) = \dfrac{m_{AuNP}}{m_{QR}} \end{cases}.$$

The number of AuQDs per QR, n_{AuQD} was then induced from the mass of AuQDs per QR, m_{AuQD}, using

$$\begin{cases} m_{Au_nQD} = n \cdot \dfrac{M_{Au}}{\mathcal{N}_a} \\ n_{AuQD} = \dfrac{m_{AuQD}}{m_{Au_nQD}} \end{cases}$$
$$\Rightarrow n_{AuQD} = \frac{m_{AuQD} \cdot \mathcal{N}_a}{n \cdot M_{Au}},$$

where m_{Au_nQD} is the mass of one AuQD composed of n gold atoms. $\mathcal{N}_a$ and M_{Au} are Avogadro's number (6.02×10^{23} mol^{-1}) and the molar mass of gold (196.96 g·mol^{-1}), respectively.

SI Particle Properties

Photonic Characterization. The photonic properties of the QRs and in particular the extinction and photoluminescent properties were assessed by UV-visible and steady-state photoluminescence spectroscopy. UV-visible measurements were collected using a 1-cm path-length quartz cuvette in a PerkinElmer Lambda 25 UV-visible spectrophotometer at a scanning rate of 480 nm·min^{-1} from 400 nm to 1,000 nm with 0.2-nm resolution. Spectra were normalized to the peak maximum intensity at 672 nm. Samples were dispersed in ethanol (1 mg·mL^{-1}) and sonicated for 5 min before analysis. Samples dispersed in solvent the longest showed the sharpest peak.

Steady-state photoluminescence measurements were collected using a 1-cm path-length quartz cuvette using a Horiba Scientific Fluorolog-3 (FL3-21) spectrophotometer with an integration time of 1 s and 12-nm slits for the QRs and 5 nm for the controls. Emission spectra were collected from 700 nm to 900 nm with an excitation at 672 nm. Excitation spectra were collected from 550 nm to 800 nm by acquiring the emission intensity at 827 nm. The acquired spectra were corrected for variations in lamp and detector efficiency and normalized to either the peak maximum for the QRs and the NQRs or the maximum in the range scanned for the controls. QR samples were dispersed in ethanol (1 mg·mL^{-1}) and sonicated for 5 min before analysis.

The quantum yield (QY) of the QRs was calculated relative to adsorption-matched dilutions of Qdot 705 ITK (Invitrogen) organic quantum dots ($QY = 0.63$) in hexane. The extinction E of both the reference Qdot and the QRs was adjusted to be below 0.2 optical density at the excitation wavelength (672 nm) for the QRs and at the adsorption maximum of the Qdot (450 nm) for the reference Qdot to minimize luminescence quenching due to internal reabsorption. The final QY of the QRs was calculated according to

$$QY = QY_{ref} \frac{I}{I_{ref}} \frac{n^2}{n_{ref}^2} \frac{\left(1 - 10^{-E}\right)^{ref}}{1 - 10^{-E}},$$

where n is the refractive index, I is the integrated luminescence intensity and *ref* denotes the reference sample (the Qdot 705 ITK in this study).

Magnetic Characterization. Magnetic measurements were carried out using a Quantum Design MPMS-5S SQUID magnetometer. The field dependence of the magnetization (M vs. H) was measured for both QR and HS samples at 2 K. The samples were placed in gelatin capsules in powder form, under atmospheric conditions before being inserted in the sample space of the magnetometer. The observed saturation magnetic moment for the QRs was 0.009 μ_B per gold atom or 6,556 μ_B per particle. In comparison with QRs, the HS sample showed a weak paramagnetic behavior with an observed saturation magnetic moment of 7.5×10^{-5} μ_B per silica molecule, which was a very negligible contribution to the overall magnetism exhibited by the QRs. The calculations were based on the assumptions that the size of each QR is 150 nm with a uniform mesoporous silica shell thickness of 25 nm. All of the QRs were assumed to constitute 27% weight of AuNPs and AuQDs and 73% weight of the mesoporous silica occupying them.

Drug Loading and Release Studies.

DOX loading experiments.

Fluorescence spectroscopy. Stock solutions of QR, NQRs, or HSs were prepared by dispersing them in MilliQ H_2O at a concentration of 5 mg·mL^{-1}. Six different stock solutions of DOX were prepared in MilliQ H_2O ranging from 1 mg·mL^{-1} to 31.3×10^{-3} mg·mL^{-1} in concentration. Samples for the drug-loading experiments were obtained by adding 10 μL of stock particle dispersions to 50 μL of stock DOX solutions and 40 μL of MilliQ H_2O, resulting in a final particle concentration of 0.5 mg·mL^{-1} and a DOX concentration range of 0.5 mg·mL^{-1} to 15.6×10^{-3} mg·mL^{-1}. The samples were left to rotate overnight in the dark at room temperature. Afterward, the samples were washed three times in MilliQ H_2O at 20,817 × g and resuspended in MilliQ H_2O. The fluorescence emission of the loaded QRs or HSs particles was monitored at 590 nm with an excitation wavelength set at 470 nm using a microplate reader (SpectraMax M5). From the fluorescence results, the amount of DOX was calculated using a DOX standard curve constructed from DOX dilution series ranging from 3.91×10^{-3} mg·mL^{-1} to 2.56×10^{-6} mg·mL^{-1} in concentration. No point higher than 10 μM (5.44×10^{-3} mg·mL^{-1}) was used to construct the standard curve because above 10 μM of DOX, DOX molecules have been shown to self-associate, resulting in quenching (2). Therefore, the linear behavior of the fluorescence emission of DOX with regards to concentration can only be assumed for concentrations lower than 10 μM. The loading content was expressed as the ratio of DOX loaded in the particles to the mass of particles. The experiment was run in triplicate and the results are presented as averages ± SD. Statistical analyses were performed using MATLAB R2012a (MathWorks). A one-way ANOVA combined with a post hoc Tukey–Kramer multiple comparisons test was used to statistically assess differences in DOX loading content between the QRs, NQRs, and HSs. These differences were then deemed significant if the probability of the results occurring by random chance was less than 5% ($P < 0.05$).

TGA. QRs and HSs (20 mg) were dispersed in MilliQ H_2O (9.5 mL). DOX (5 mg or 20 mg) was dissolved in the previous solutions resulting in ratios of DOX to particles of 1:4 wt/wt or

1:1 wt/wt. The vessels were wrapped in foil to eliminate light and the solutions were stirred for 24 h. Particles were centrifuged at 20,817 × *g* for 5 min, the supernatants were decanted, and the particles were redispersed in MilliQ H_2O and immediately centrifuged under the same conditions. The supernatants were decanted again and the particles were dried at 70 °C overnight. The TGA program was as follows: Temperature was raised by 5 °C·min^{-1} up to 1,000 °C under a steady airflow.

Loading efficiency. The loading of DOX in the particles (QRs and HSs) was performed similarly to the TGA study (i.e., DOX to particle ratio of 1:4 wt/wt or 1:1 wt/wt in MilliQ H_2O). After stirring the samples in the dark for 24 h, they were centrifuged at 20,817 × *g* for 5 min. The supernatant were collected and the residual DOX content was measured by UV-visible measurements at a wavelength of 480 nm. The loading efficiency (L_{eff}) were calculated as follows:

$$L_{eff} = \frac{A_{init} - A_{res}}{A_{init}},$$

where A_{init} is the absorption value at 480 nm of the initial DOX solution and A_{res} is the absorption value at 480 nm of the residual DOX in the supernatant after the particles were loaded.

DOX release experiments. Stock solutions of QRs, NQRs, or HSs were prepared by dispersing them in MilliQ H_2O at a concentration of 5 mg·mL^{-1}. A stock solution of 1 mg·mL^{-1} of DOX was prepared in MilliQ H_2O. Samples for the drug-loading experiments were obtained by adding 10 μL of stock particle dispersions to 50 μL of stock DOX solutions and 40 μL of MilliQ H_2O, resulting in a final particle concentration of 0.5 mg·mL^{-1} and DOX concentration of 0.5 mg·mL^{-1}. The samples were left to rotate overnight in the dark at room temperature. Afterward, the samples were washed three times in MilliQ H_2O at 20,817 × *g*, resuspended in PBS (PBS, pH 7.4), and left to rotate in the dark at room temperature. At 0.5, 1, 2, 4, 8, 12, 24 and 48 h, the supernatants of the samples were collected by centrifuging the samples at 20,817 × *g* for 5 min. The particles were resuspended in PBS and the fluorescence emission of the collected supernatant was monitored at 590 nm with an excitation wavelength set at 470 nm using a microplate reader (SpectraMax M5). From the fluorescence results, DOX release from the DOX-loaded particles was calculated using a DOX standard curve constructed from DOX dilution series ranging from 3.91×10^{-3} mg·mL^{-1} to 2.56×10^{-6} mg·mL^{-1} in concentration. The DOX release profile shows the normalized value of the accumulated mass of DOX released by the particles over time. The experiment was run in triplicate and the results are presented as averages ± SD.

EasyPlot was used to model the drug release data. A pseudo-second-order rate equation was used to fit the data:

$$q_t = \frac{kq_e^2 t}{(1 + kq_e t)},$$

where q_t is the amount of DOX desorbed at time t, t is time in hours, q_e is the amount of DOX desorbed at equilibrium, and k is the overall rate of adsorption. The initial rate of adsorption (h_0) was then calculated from the obtained k and q_e values; $h_0 = kq_e^2$.

Statistical analyses were performed using MATLAB R2012a (MathWorks). A one-way ANOVA combined with a post hoc Tukey–Kramer Multiple comparisons test was used to statistically assess differences in DOX release kinetics between the QRs, NQRs, and HSs. These differences were then deemed significant if the probability of the results occurring by random chance was less than 5% ($P < 0.05$).

Cell culture. The human cervical cancer HeLa cells used in this study were obtained from European Collection of Cell Cultures. The cells were maintained in an incubator at a temperature of 37 °C, regulated with 5% CO_2 and 95% air, and a saturated humidity. DMEM supplemented with 10% (vol/vol) FBS (Gibco) and 1% (vol/vol) antibiotic–antimycotic was used as the cell culture medium. The cell media was changed every 2–4 d and the cells were passed using trypsin– EDTA upon reaching 80% confluency.

QRs' drug delivery performance in vitro.

DOX delivery to cells. QRs were loaded with DOX overnight as described in *SI Particle Properties*, *DOX loading experiments*, achieving quantitative loading to provide the desired final concentration of DOX. HeLa cells were seeded at a density of 2·10^4 cells·cm^{-2} in 48-well plates (Corning). After 1 d, DMEM was prepared with the six chosen concentrations of free DOX or QR-encapsulated DOX and the nontreated control. The medium was added to the cells and allowed to incubate for 6 h. The cells were thoroughly washed with PBS, trypsinized, and collected in flow cytometry tubes containing 1 mL of 1% (vol/vol) paraformaldehyde (PFA) in PBS. Following 15-min fixation, the DOX fluorescence within the cells was immediately analyzed by flow cytometry with 488-nm excitation laser and 595-nm emission filter. The experiment was performed four times.

Cytotoxicity of DOX-loaded QRs. QRs were loaded with DOX overnight as described in *SI Particle Properties*, *DOX loading experiments*, achieving quantitative loading to provide the desired final concentration of DOX. HeLa cells were seeded at a density of 2·10^4 cells·cm^{-2} in 48-well plates (Fisher Scientific). After 1 d, DMEM was prepared with the six chosen concentrations of free DOX or QR-encapsulated DOX and the nontreated control. The medium was added to the cells and allowed to incubate for 1 d. After washing the cells thoroughly with PBS, 300 μL of phenol red-free, HEPES-buffered DMEM containing 10% (vol/vol) AlamarBlue (Life Technologies) was added to each well. The AlamarBlue assay was incubated for 1 h in a cell culture incubator. The fluorescence originating from each well was measured by microplate reader with 545-nm excitation and 590-nm emission. The data are reported as the percentage of substrate conversion with respect to the untreated control. The experiment was performed four times.

SI QRs' Cytotoxicity

MTT Assay. HeLa cells were cultured in 48-well plates (Fisher Scientific). Briefly, the cells were seeded at a density of 2·10^4 cells·cm^{-2} and cultured for 1 d with NPs at a concentration of 10^{11} particle·mL^{-1}. The cells were then incubated in a cell culture incubator at 37 °C with 5% CO_2 for 1 d or 3 d. Afterward, the media containing the particles was removed, and 300 μL of 3-[4,5-dimethylthiazol-2-yl]-2,5-diphenyltetrazolium bromide (MTT) salt solution (diluted in a culture media without red phenol and with a final concentration of 0.5 mg·mL^{-1}) was added. After another 2-h incubation time at 37 °C, the media was replaced with 300 μL of DMSO per well, and the absorbance was monitored using a microplate reader (SpectraMax M5) at the wavelength of 570 nm with a reference wavelength at 650 nm. The cytotoxicity was expressed as the percentage of cell viability compared with each time point's respective untreated cell controls. The experiment was run in triplicate and the results are presented as percentage averages ± SD.

The negative and positive controls were medical grade PVC and organo-tin PVC, respectively, which are used in ISO 10993-5 cytotoxicity tests. Both plastic materials were left in 70% (vol/vol) ethanol for 2 h and thoroughly washed in PBS and media. Media (0.2 mL·cm^{-2} of plastic control material) was added to dry samples of both control materials and left in the incubator for 1 d. The media obtained was then used in the same way as the particle containing sample media.

Total DNA Assay. HeLa cells were cultured in 48-well plates (Fisher Scientific). Briefly, the cells were seeded at a density of 2·10^4 cells·cm^{-2} and cultured for 1 d with NPs at a concentration of

10^{11} particle·mL^{-1}. The cells were then incubated in a cell culture incubator at 37 °C with 5% CO_2 for 1 d or 3 d. At the end of the incubation, DNA was extracted from the cells lysed by incubating them in papain digest (5 mM cystein·HCl, 5 mM EDTA, and 1 unit·mL^{-1} of papain in PBS) for 2 h in 5% CO_2 at 60 °C. A 20-fold dilution of the TE buffer (10 nM Tris·HCl and 1 mM EDTA) from the Quant-iT PicoGreen dsDNA (tDNA) assay kit was prepared to make the working solution of PicoGreen reagent (200-fold dilution in TE). The working reagent was added to the lysate and allowed to react for 5 min in the dark. The fluorescence emission was monitored at 535 nm with an excitation wavelength set at 480 nm using a microplate reader (SpectraMax M5). The cytotoxicity was expressed as the concentration of double-stranded DNA, which was calculated by subtracting the values obtained for DNA cell-free controls against a DNA standard curve constructed from known DNA concentrations. The negative and positive controls are identical to the controls prepared for the MTT assay described previously. The experiment was run in triplicate and the results are presented as percentage averages ± SD.

SI QR Internalization Studies

Laser Confocal Scanning Microscopy. HeLa cells were cultured in eight-well glass chamber slides (Lab-Tek). Briefly, the cells were seeded at a density of $2{\cdot}10^4$ cells·cm^{-2} and cultured for 1 d with nanoparticles (NPs) at a concentration of 10^{11} particle·mL^{-1}. After the medium was removed, the cells were washed 3 times with PBS and fixed with 4% (vol/vol) PFA in PBS. The cells F-actin and nuclei were stained with AlexaFluor 488 phalloidin (AF488 phalloidin, Invitrogen) and DAPI, respectively, using established methods. The cells were first permeabilized using 0.1% (vol/vol) Triton X in PBS for 5 min. The cell samples were then blocked with 1% (wt/vol) BSA (BSA) in PBS for 30 min. The phalloidin and DAPI solutions were added under dark conditions for 30 min and 5 min, respectively. In between each step the samples were washed twice with PBS. The QRs were observed using a multiphoton NIR laser. The glass slides were visualized under a confocal microscope (Leica SP5 MP/Flim inverted) and the images were analyzed with Volocity 6.0 (PerkinElmer) and Amira 3D visualization software (Mercury Computer Systems). The 3D confocal internalization movie was edited using iMovie (Apple).

Electron Microscopy. HeLa cells were cultured in 24-well plates (Fisher Scientific). Briefly, the cells were seeded at a density of $2{\cdot}10^4$ cells·cm^{-2} and cultured for 1 d with NPs at a concentration of 10^{11} particle·mL^{-1}. After the medium was removed the cells were detached by incubation with 0.25% (vol/vol) trypsin–EDTA for 5 min. The cell suspension was centrifuged at 151 × *g* for 5 min. The supernatant was removed and the cells were fixed on ice by 2.5% (vol/vol) glutaraldehyde and 0.1 M cacodylate buffer in MilliQ water for 30 min. Further fixation with 2% (wt/vol) osmium tetroxide and 2% (wt/vol) potassium ferrocyanide in 0.1 M cacodylate buffer also provided heavy metal contrast staining for electron microscopy visualization of cells. The cells were dehydrated through a graded ethanol series and then washed twice in 100% acetone. The embedding was performed through a graded Epon812/Araldite resin:acetone series (1:2, 2:1, 1:0 vol/vol), transferred to fresh pure Epon812/Araldite, and polymerized at 60 °C for 1 d. Ultrathin sections of ∼100 nm were cut on a Power Tome XL ultramicrotome (RMC Products) using a 45° diamond knife (Diatome) and transferred to a 300-mesh thin bar TEM copper grids (Electron Microscopy Sciences). TEM images of more than 30 different cells were acquired using a JEOL 2000 TEM equipped with EDS detector, operated at 120 kV.

SI Assessment of the QR's Photothermal Performance in Vitro

LIVE/DEAD Assay. HeLa cells were cultured in 24-well plates (Fisher Scientific). Briefly, the cells were seeded at a density of $2{\cdot}10^4$ cells·cm^{-2} and cultured for 1 d with NPs at a concentration of 10^{11} particle·mL^{-1}. At the end of the incubation period, samples were irradiated with a 300-mW, 671-nm laser (38 W·cm^{-2}) for 0, 2, 5, 8, 10, and 15 min. The total amount of time outside the incubator for any sample was 15 min. Afterward, the media containing the particles was removed, and 1 mL of LIVE/DEAD solution (2 μM calcein AM and 2 μM ethidium homodimer-1 in PBS (Invitrogen) was added. The samples were incubated for another 45 min at 37 °C before being imaged using a Leica epifluorescent inverted microscope. The LIVE green and DEAD red images were merged using Photoshop CS5 (Adobe) to obtain the LIVE/DEAD images used to quantify cell death. The experiment was performed four times.

LIVE/DEAD Assay Quantification. Image processing and segmentation algorithms were used to quantify the QR-mediated cell death. Masks were applied to the fluorescent microscopy images in Photoshop CS5 (Adobe) to obtain the exact areas of the irradiated cell population. The inverse of a 1-mm disk centered on the laser spot was used as a mask to obtain the irradiated cell population. The images of both LIVE and DEAD channels were then segmented using MATLAB R2012a (MathWorks) to obtain binary images representing the surface of live and dead cells, respectively. The percentage cell death was obtained by calculating the sum of the binary image matrices and normalizing the DEAD channel value over the total of both LIVE and DEAD channel values. The experiment was run in quadruplicate and the results are presented as averages ± SD. Statistical analysis was performed using MATLAB R2012a (MathWorks). A one-way ANOVA combined with a post hoc Tukey–Kramer multiple comparisons test was used to statistically assess differences in cell death at different NIR irradiation time treatments between the QRs and between the QRs, HSs, and no-particle controls at the initial and final time points. These differences were then deemed significant if the probability of the results occurring by random chance was less than 1% ($P < 0.01$).

SI QR's Treatment Performance in Vivo

Animal Model for Evaluating QR-Mediated Therapy.

Tissue culture. LS174T human colorectal carcinoma cells were stably transduced to express firefly luciferase coexpressing truncated CD34 (3) (LS174T-luc) in Martin Pule's laboratory. Briefly, RD114-packaged retrovirus was created by transient transfection of 293T cells and this was used to transduce 2.5×10^4 cells by the addition of 1 μg·mL^{-1} polybrene. Cells were grown in T175 flasks (Fisher Scientific) in DMEM, supplemented with 10% heat-inactivated FCS (GIBCO) in a humidified incubator at 37 °C with 5% CO_2 and 95% air.

Animal model. All animal studies were approved by the University College London Biological Services Ethical Review Committee and licensed under the U.K. Home Office regulations and the Guidance for the Operation of Animals (Scientific Procedures) Act 1986 (Home Office, London, United Kingdom). Seven female adult (6–8 wk) CD1 nu/nu mice (Charles Rivers) were anesthetized using 2% (vol/vol) isoflurane in O_2 and received s.c. injections of 5×10^6 LS174T-luc cells in 100 μL serum-free DMEM into the right flank. Animal weights and tumor volumes were recorded every 2 d using calipers once the tumors became palpable and the volume was estimated assuming an ellipsoid shape using the following equation: volume = length × width × depth × π/6. Once tumors reached 500 mm^3, which took ∼14 d, the tumors were large enough for QR imaging and treatment regimes.

QR As Imaging Agent in Vivo.

Fluorescence imaging. Fluorescent images were acquired using an IVIS Lumina II Bioluminescent scanner (Caliper Life Sciences). QRs or HSs (100 μL, 5.7×10^{12} particle·mL^{-1}) were injected interstitially into the tumor volume of an anesthetized mouse [2% (vol/vol) isoflurane in O_2]. Approximately 1 h after injection, the mice were imaged with the IVIS Lumina II scanner set to fluorescence mode with luminescent exposure times of 30 s and Cy5.5 excitation and ICG emission filters (QR $n = 3$, HS $n = 3$). Mice were anesthetized with 2% (vol/vol) isoflurane in O_2 before and during imaging; body temperature was maintained using a hot air system and the animals were monitored throughout. The background autofluorescence was removed by applying a threshold in ImageJ (National Institutes of Health).

MRI. Magnetic resonance images were acquired using a 9.4T Agilent VNMRS scanner. Solutions of QRs were prepared at concentrations of 0.01, 0.1, 1, and 10 mg·mL^{-1} and placed in the center of the MRI scanner. Longitudinal relaxation rates (R_1) for each sample were estimated from images acquired using a multislice, segmented Look–Locker sequence. Sequence parameters included a field of view of 30×30 mm^2, matrix size of 128×128, five slices, 1-mm slice thickness, echo time of 1.18 ms, TI of 110 ms, time between readout pulses of 2.3 ms, readout flip angle of 8°, repetition time of 13 s, and 50 inversion recovery readouts. A three-parameter exponential function was fitted to the data, on a pixel-by-pixel basis, from which the average R_1 from each sample was estimated. The change in R_1 was plotted against the logarithm of the concentration. For in vivo MRI measurements the mouse was anesthetized using isoflurane in O_2 [3% (vol/vol) for induction, 1.2% (vol/vol) for maintenance] and placed in the center of the MRI scanner (QR $n = 1$). The s.c. tumor was first set in dental paste to minimize motion. Core temperature was monitored and maintained at 37 °C using a warm air blower. A 39-mm radiofrequency coil was used for transmission and reception (Rapid Biomedical). Look–Locker data were acquired using the same sequence as used when imaging samples in vitro and fitted to the same three-parameter model to estimate R_1. QRs (200 μL, 5.7×10^{12} particle·mL^{-1}) were then injected directly into the tumor and a second set of Look–Locker data was acquired. An image was produced showing the change in R_1 from baseline in pixels inside a region of interest (ROI) corresponding to the tumor, which was overlaid on a greyscale morphological image.

Photoacoustic imaging. Photoacoustic signals were acquired using an all-optical, backward mode, planar photoacoustic scanner based upon an FP polymer film ultrasound sensor (4). QRs (100 μL, 5.7×10^{12} particle·mL^{-1}) were injected interstitially into the tumor volume of a mouse anesthetized using isoflurane in O_2 [4% (vol/vol) for induction, 1.5% (vol/vol) for maintenance] (QR $n = 1$). The mouse was then placed on the FP sensor head. Ultrasound matching gel or water was used to provide acoustic coupling between the skin and sensor. The entire imaged area (14×14 mm^2) was illuminated with an incident surface fluence of less than 10 mJ·cm^{-2} using 7-ns optical pulses emitted by a tunable OPO laser system (Quanta Ray Pro-270/premiScan; Newport Spectra Physics/GWU). The photoacoustic scanner therefore operates in the tomography mode, in which an imaging depth of up to 1 cm with sub-100 μm spatial resolution is achievable (4). A typical scan acquired 20,000 waveforms, each of which contained 640 time points, and took about 8 min to complete. Three-dimensional photoacoustic images were reconstructed from the detected waveforms, using a time reversal algorithm with correction for acoustic attenuation in tissue. The image reconstruction algorithm was implemented using k-Wave, an open source MATLAB toolbox developed at University College London for the time-domain simulation and reconstruction of photoacoustic and ultrasound wave fields (www.k-wave.org). The sound speed used in the reconstruction was selected using an autofocus approach. To aid visualization of deeper-lying features, the image intensity was normalized with respect to depth using an exponential function as a first-order correction for optical attenuation and the reconstructed 3D images interpolated three times onto a finer x–y grid. The segmentation of the QRs in the reconstructed image was achieved using the threshold segmentation tool in Amira (FEI Visualization Sciences).

QR's Performance as Therapy Agent in Vivo. Mice were anesthetized with 2% (vol/vol) isoflurane. Approximately 1 h after injection (100 μL, 5.7×10^{12} particle·mL^{-1}, QR $n = 3$, HS $n = 3$), the tumors were imaged for bioluminescence expression 15 min after an aqueous solution of D-luciferin (Regis Technologies Inc.) at 150 mg·kg^{-1} in a volume of 200 μL was injected intraperitoneally. Imaging was performed using an IVIS Lumina II Bioluminescent scanner (directly after fluorescence imaging) with a 2-s exposure time. At 3 h after injection, tumor sites were exposed to NIR light (671 nm, 0.9 W·cm^{-2}, 5-mm spot diameter) for 15 min and the temperature profiles were monitored by using an Infratec VarioCAM hr 780 IR thermal camera with a 30-mm close-up lens. The infrared frames were captured at a rate of 25 Hz with an optical resolution of 40 μm for the duration of the exposure. Data were logged for more than 15 min with the maximum temperature in disk area centered on the injection site was recorded. The experiments were repeated in three different mice for each sample group. The surface and actual body temperature of the mouse was recorded separately. At 24 h after exposure to NIR light the animals were scanned for bioluminescence as before. The mice were then killed by schedule 1 method and the tumors were removed for histology.

Bioluminescent assay quantification. Quantification of the bioluminescent signal was performed using an ROI covering the spot exposed to NIR light area using Living Image software (version 4; Caliper Life Sciences).

Histology. Tumors where fixed in 4% (vol/vol) formalin for 4 h at 4 °C and then incubated overnight in 15% (wt/vol) sucrose in PBS at 4 °C. Tissue was dehydrated in 70% (vol/vol) ethanol and embedded in paraffin. Sections were cut at 5 μm and then stained with hematoxylin for 1 min and eosin for 30 s and images were obtained using a Hamamatsu NanoZoomer 2.0-HT Slide Scanner (Hamamatsu Japan) with NanoZoomer Digital Pathology NDP.view software (Hamamatsu Japan).

SI Results and Discussion

Characterization of Silica Shells and QRs. The nitrogen adsorption and desorption isotherms of the QRs were type IV isotherms characteristic of mesoporous materials (1). The large box-like hysteresis observed in the isotherms is indicative of a macrocavity accessible only through small bottleneck pores (1). The presence of such a hysteresis curve indicates that the integrity of the silica shells was not compromised or cracked during the incorporation of gold clusters (Fig. S3*A*). However, the mesopore volume of the shell, originally 1.43 cm^3·g^{-1}, decreased to 0.19 cm^3·g^{-1} on the formation of the QRs. Considering that the total AuQD volume (calculated assuming 18 thiol ligands around a 1-nm-diameter AuQD) amounts to 0.14 cm^3·g^{-1}, this decrease can only be explained by mesopore blocking. Consistent with the decrease in mesopore volume, there is a disappearance of the larger mesopores in the pore size distribution (Fig. S3*B*). The pore structure within the silica shells of the QRs was confirmed by SAXS (Fig. S3*C*). A d spacing of 4.6 nm was found for the HSs, which did not change upon incorporation of gold.

AuQD Properties. Other research groups have studied the optical absorption spectrum of AuQDs by performing DFT calculations (5). The calculated spectrum of stable AuQDs consisting of 25 atoms [$Au_{25}(SR)_{18}$] showed extinction spectra similar to that of

the QRs, whereas larger AuQDs do not (5, 6). Zhu et al. (5) stated that the 670-nm peak corresponded to the LUMO ← HOMO transition, which was essentially an intraband (sp ← sp) transition. The 411-nm peak was harder to assign because the DFT calculations reported peaks at 400 nm and 450 nm. Although there was a shoulder around 450 nm in the extinction spectrum of the QRs, the only distinct peak appeared at 411 nm. The lack of peaks could be the result of the interference from the plasmon resonance of the larger gold nanoparticles (AuNPs) inside the QRs' silica shells that probably red-shifted the 400-nm and attenuated the 450-nm peaks. However, another study on 11-atom AuQDs ($Au_{11}C_{12}$) showed identical extinction spectra (7), which seems to imply that the QRs could also be populated by 11-atom AuQDs or a mixture of the two.

1. Blas H, et al. (2008) Elaboration of monodisperse spherical hollow particles with ordered mesoporous silica shells via dual latex/surfactant templating: Radial orientation of mesopore channels. *Langmuir* 24(22):13132–13137.
2. Karukstis KK, Thompson EH, Whiles JA, Rosenfeld RJ (1998) Deciphering the fluorescence signature of daunomycin and doxorubicin. *Biophys Chem* 73(3):249–263.
3. Fehse B, et al. (2000) CD34 splice variant: An attractive marker for selection of gene-modified cells. *Mol Ther* 1(5 Pt 1):448–456.
4. Laufer J, et al. (2012) In vivo preclinical photoacoustic imaging of tumor vasculature development and therapy. *J Biomed Opt* 17(5):056016–0560168.
5. Zhu M, Aikens CM, Hollander FJ, Schatz GC, Jin R (2008) Correlating the crystal structure of a thiol-protected Au25 cluster and optical properties. *J Am Chem Soc* 130(18): 5883–5885.
6. Qian H, Zhu M, Wu Z, Jin R (2012) Quantum sized gold nanoclusters with atomic precision. *Acc Chem Res* 45(9):1470–1479.
7. Yang Y, Chen S (2003) Surface manipulation of the electronic energy of subnanometer-sized gold clusters: An electrochemical and spectroscopic investigation. *Nano Lett* 3(1): 75–79.

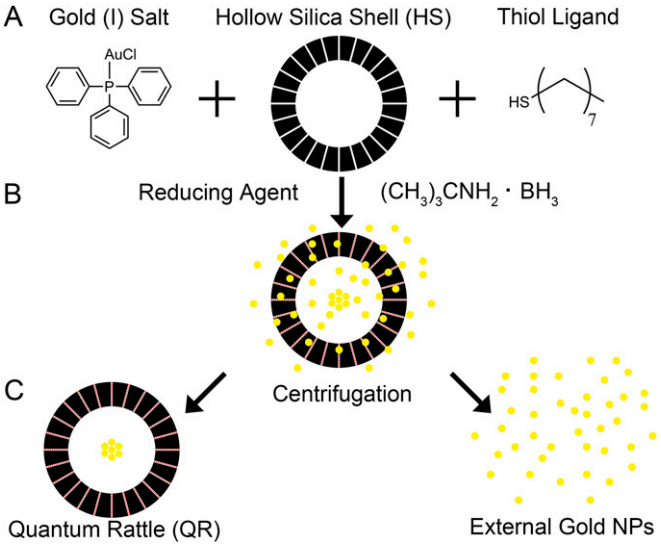

Fig. S1. Schematic of QR synthesis. (*A*) Chloro(triphenylphosphine) gold (I) salt and 1-octanethiol are infused into hierarchically porous silica shells (HS). (*B*) Nucleation and formation of AuQDs (red) inside the mesopores of the silica shell and AuNPs (yellow) inside and outside the hollow shell following the addition of the borane *tert*-butylamine complex reducing agent. (*C*) Purification step separating QRs from gold nanoparticles formed outside the hollow silica shells.

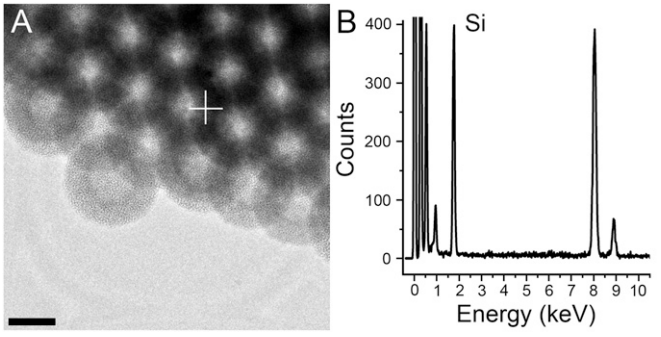

Fig. S2. QR synthesis using gold (III) salt as metallic precursor. (*A*) Bright field TEM image showing a hollow mesoporous silica shell without any gold nanostructures inside the cavity. The white cross indicates where EDS analysis was performed. (Scale bar, 100 nm.) (*B*) Corresponding EDS spectrum showing no elemental trace of gold (expected peaks at 2.41 keV and 9.71 keV).

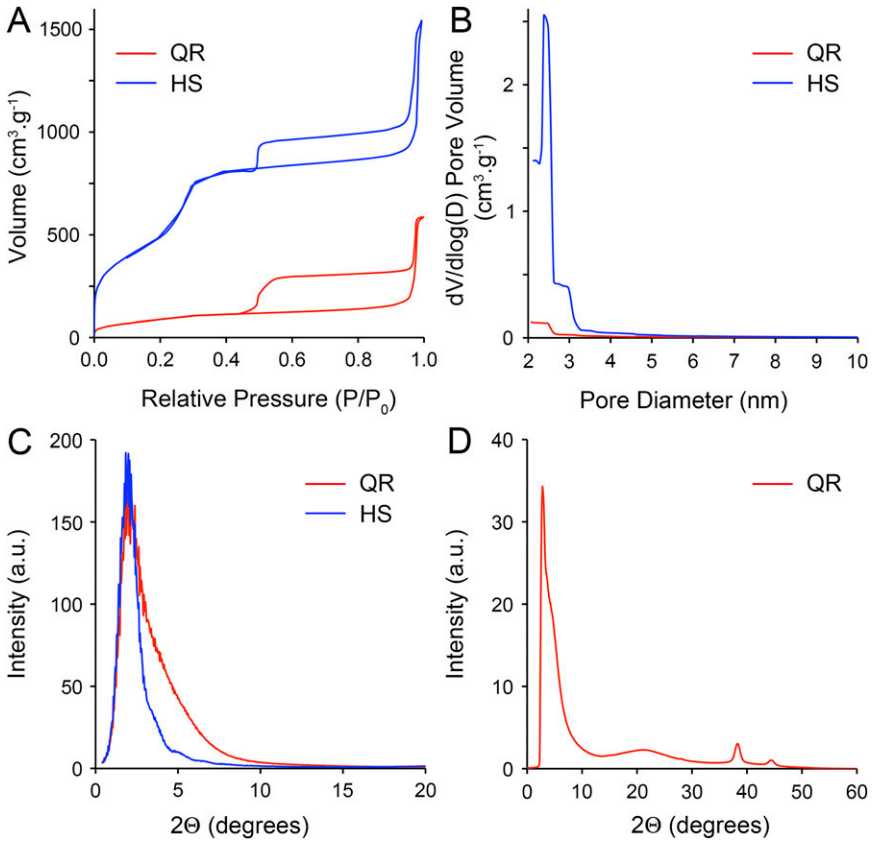

Fig. S3. Characterization of silica shells and QRs. (*A–D*) Nitrogen adsorption and desorption isotherm (*A*), Barrett Joyner Halenda pore size distribution (*B*), SAXS, and (*C*) WAXS (*D*) of QRs (red) and mesoporous silica shells (HS, blue).

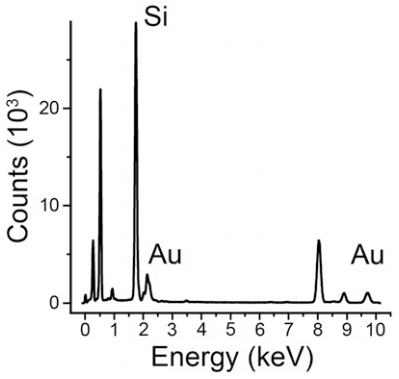

Fig. S4. QR elemental analysis. Representative energy-dispersive X-ray spectrum of QRs indicating the presence of silicon and gold (ratio Au:Si is equal to 0.37).

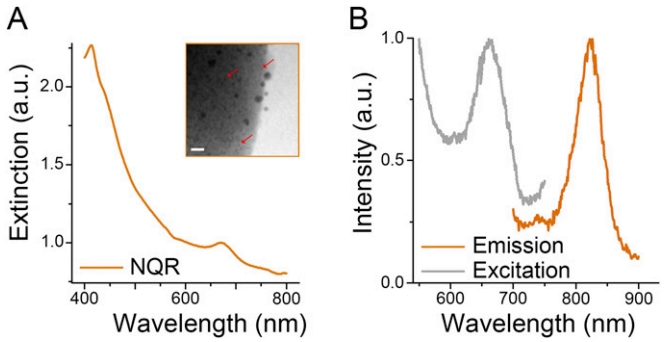

Fig. S5. Photonic properties of NQRs. (*A*) Extinction spectrum of NQRs (orange) showing the same characteristic features as the QR extinction spectrum. (*Inset*) Bright field TEM of the AuQDs (red arrows) within the NQR. (Scale bar, 10 nm.) (*B*) Photoluminescence spectra of NQRs showing an excitation peak centered at 672 nm and an emission peak centered at 827 nm. Both emission spectrum (λ_{ex} = 672 nm, orange) and excitation spectrum (λ_{em} = 827 nm, gray) are similar to the QRs' photoluminescent spectra.

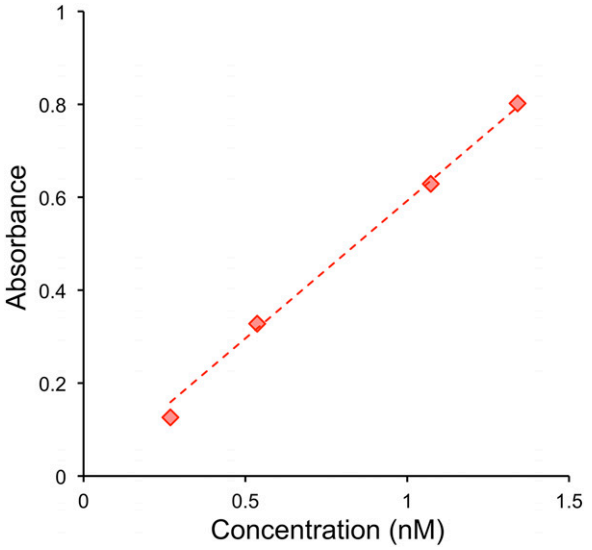

Fig. S6. QRs' photonic properties: molar extinction coefficient. Plot of the absorbance at 672 nm vs. QR concentration showing that the absorbance value is linearly proportional to the QRs' concentration. A linear regression was applied (R^2 of 0.995) to determine the QRs' molar extinction coefficient at 672 nm, which was calculated to be 5.9×10^8 $M^{-1}{\cdot}cm^{-1}$.

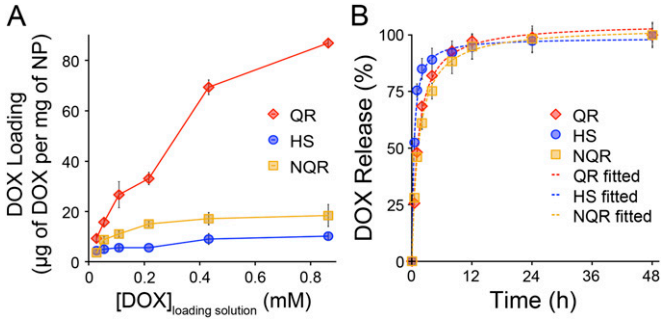

Fig. S7. Loading and release of DOX. (*A*) Plot of the DOX loading amount against DOX concentration of the loading solution showing up to ninefold and fivefold increase in the amount of DOX loaded in the (QRs (red) compared with the hollow mesoporous silica shells (HS, blue) and the NQRs (orange), respectively. (*B*) Drug release profile of QRs (red) compared with HSs (blue) and NQRs (orange). The NQRs exhibit a drug-release profile that is similar to that of the QRs with a prolonged release compared with HSs, where the DOX release plateaus earlier. A pseudo-second-order sorption model was applied (R^2 of 0.99) to the drug release profiles (dotted lines), indicating a relatively strong attraction between the silica substrate and DOX. Error bars represent the SD of triplicate experiments.

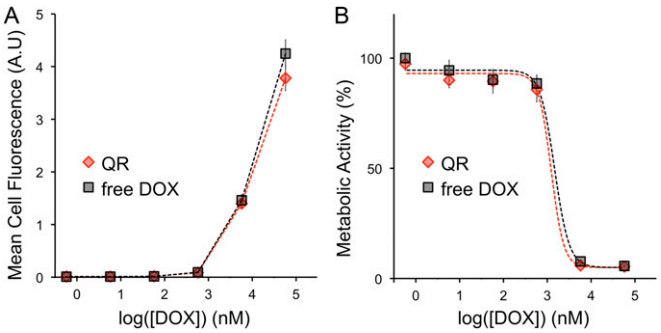

Fig. S8. QRs' drug-delivery performance in vitro. (*A*) Plot of the geometric mean fluorescence measured by flow cytometry for cells incubated with DOX from DOX-loaded QRs (red) compared with free DOX (black) showing similar profiles. Cell fluorescence is proportional to DOX uptake. (*B*) Plot of the cytotoxicity of DOX-loaded QRs (red) compared with free DOX (black) showing similar cytotoxicity profiles, with an IC_{50} of 1,468 nM and 1,229 nM for DOX and DOX-loaded QRs, respectively. Error bars represent the SDs of quadruplicate experiments.

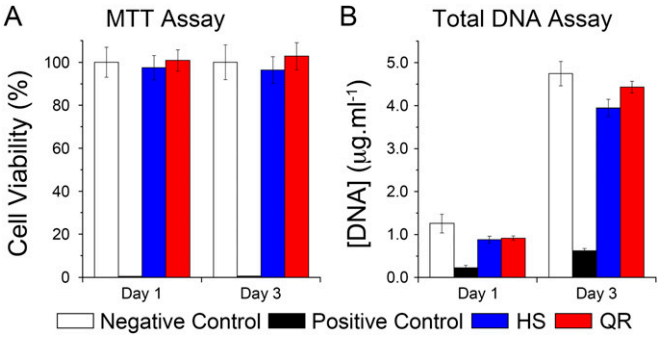

Fig. S9. QRs' cytocompatibility. (*A*) MTT assay of HeLa cells after 1 d and 3 d incubation in media containing QRs (red) or hollow mesoporous silica shells (HS, blue) do not show alterations of metabolic activity compared with medical-grade PVC (negative control, white), whereas no metabolic activity is measured with polyethylene (positive control, black). Results are normalized to blank control (cell culture media without nanoparticles). (*B*) Total DNA assay of HeLa cells after 1 d and 3 d incubation in media containing either QRs (red) or HSs (blue) do not show alterations of cell proliferation compared with medical-grade PVC (negative control, white). Cell proliferation and viability are significantly affected by polyethylene (positive control, black). Error bars represent the SDs of triplicate experiments.

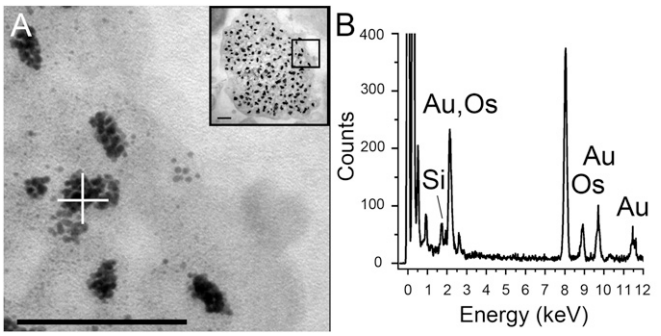

Fig. S10. QR internalization: elemental analysis. (*A*) TEMs of ultrathin sections of HeLa cells incubated with QRs for 1 d showing several QRs within a cell, where EDS analysis was performed (white cross). (*Inset*) Lower-magnification TEM image of a QR cluster inside a vesicle within the cell cytoplasm. (Scale bars, 100 nm.) (*B*) EDS spectrum of the QR region indicating the presence of silicon and gold.

Table S1. Magnetic moment of ultrasmall gold nanoparticles reported in the literature

Gold nanoparticle size, nm	Ligand	Magnetic property	Magnetic moment, μ_B	Refs.
3.5	No ligand (bare nanoparticles)	Ferromagnetic	16 per particle	(1)
2.5	Poly-N-vinyl-2-pyrrolidone (PVP)	Ferromagnetic	20 per particle	(2)
1.9	Dodecanethiol	Ferromagnetic	0.33 per atom	(3)
5	Dodecanethiol	Superparamagnetic	0.006 per atom	(4)
6.7	Oleic acid and oleylamine	Ferromagnetic	0.002 per atom	(5)
~1.4 (Au_{55})	Triphenylphosphine	Ferromagnetic	0.001 per atom	(6)
~1 (Au_{25})	Phenylethylthiol	Paramagnetic	0.002 per atom	(6)
2.1	Triphenylphosphine	Ferromagnetic	0.08 per particle	(7)
1.4	Dodecanethiol	Ferromagnetic	0.036 per atom	(8)
1.9	PAAHC (polyallyl amine hydrochloride)	Ferromagnetic	0.4 per particle	(8)
2.1	Dodecanethiol	Ferromagnetic	0.46 per particle / 0.0059 per functional group	(9)
2	Dodecanethiol	Ferromagnetic	0.005 per atom	(10, 11)
2.3	Octanethiol	Ferromagnetic	0.004 per atom	(10)
2.5	Tiopronin	Paramagnetic	0.001 per atom	(10)
1.9	Octanethiol/11-thioundecanioc acid	Ferromagnetic	0.0006 per atom	(10)
1.7	Azobenzene-thiol	Ferromagnetic	0.033 per atom (*trans*) and 0.024 per atom (*cis*)	(12, 13)

1. Wu C-M, et al. (2010) Quantum spins in Mackay icosahedral gold nanoparticles. *J Nanopart Res* 12(1):177–185.
2. Hori H, et al. (1999) Anomalous magnetic polarization effect of Pd and Au nano-particles. *Phys Lett A* 263(4-6):406–410.
3. Garitaonandia JS, et al. (2008) Chemically induced permanent magnetism in Au, Ag, and Cu nanoparticles: localization of the magnetism by element selective techniques. *Nano Lett* 8(2):661–667.
4. Dutta P, Pal S, Seehra MS, Anand M, Roberts CB (2007) Magnetism in dodecanethiol-capped gold nanoparticles: Role of size and capping agent. *Appl Phys Lett* 90:213102.
5. de la Presa P, Multigner M, de la Venta J, García MA, Ruiz-González ML (2006) Structural and magnetic characterization of oleic acid and oleylamine-capped gold nanoparticles. *J Appl Phys* 100:123915.
6. Krishna KS, Tarakeshwar P, Mujica V, Kumar CSSR (2014) Chemically induced magnetism in atomically precise gold clusters. *Small* 10(5):907–911.
7. Muñoz-Márquez MA, et al. (2010) Permanent magnetism in phosphine- and chlorine-capped gold: from clusters to nanoparticles. *J Nanopart Res* 12(4):1307–1318.
8. Crespo P, et al. (2004) Permanent magnetism, magnetic anisotropy, and hysteresis of thiol-capped gold nanoparticles. *Phys Rev Lett* 93:087204.
9. Donnio B, García Vázquez P, Gallani JL, Guillon D, Terazzi E (2007) Dendronized ferromagnetic gold nanoparticles self-organized in a thermotropic cubic phase. *Adv Mater* 19(21): 3534–3539.
10. Guerrero E, et al. (2008) Electronic structure, magnetic properties, and microstructural analysis of thiol-functionalized Au nanoparticles: role of chemical and structural parameters in the ferromagnetic behaviour. *J Nanopart Res* 10(1):179–192.
11. Crespo P, Guerrero E, Muoz-Marquez MA, Hernando A, Fernandez A (2008) Influence of the capping molecule on the magnetic behavior of thiol-capped gold nanoparticles. *IEEE Trans Magn* 44(11):2768–2771.
12. Suda M, Kameyama N, Suzuki M, Kawamura N, Einaga Y (2008) Reversible phototuning of ferromagnetism at Au-S interfaces at room temperature. *Angew Chem Int Ed Engl* 47(1): 160–163.
13. Suda M, et al. (2009) Size-reduction induced ferromagnetism and photo-magnetic effects in azobenzene-thiol-passivated gold nanoparticles. *Polyhedron* 28(9-10):1868–1874.

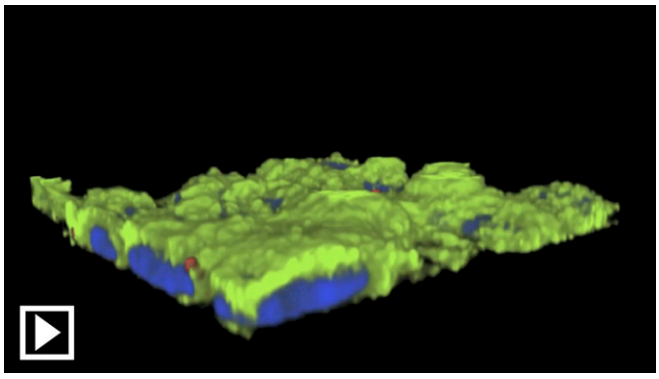

Movie S1. QR internalization and near-infrared fluorescence. Three-dimensional reconstruction of laser confocal scanning microscopy images of HeLa cells incubated for 1 d with QRs, which are imaged through their native fluorescence (red). Cells are stained for F-actin (AF488 phalloidin, green) and nucleus (DAPI, blue). QRs are localized by monitoring their native fluorescence within the cells, accumulating in the perinuclear region.

Movie S1

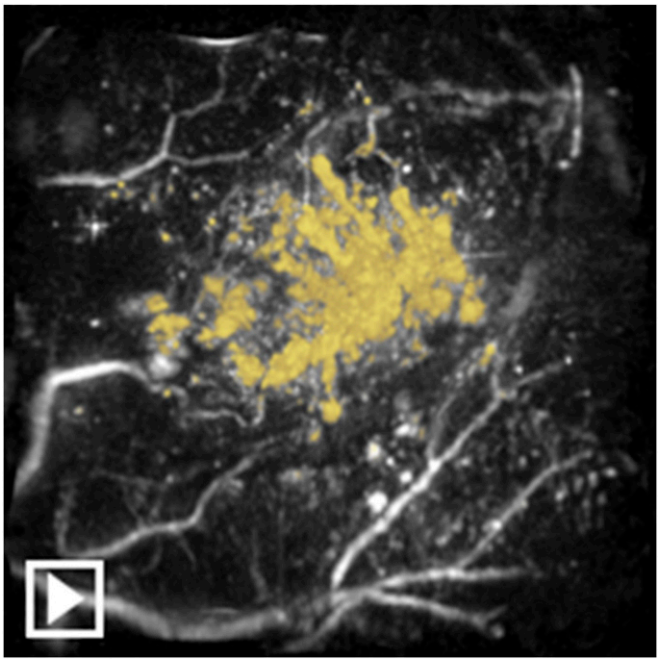

Movie S2. Three-dimensional photoacoustic imaging. Animated volume-rendered image of the dataset visualized in Fig. 4*D* showing a tumor following injection of QRs. The contrast provided by the QRs is false-colored yellow. The excitation wavelength was 670 nm.

Movie S2